Structural Analysis of a Parawing during Deployment

PAUL M. KENNER*
Vought Missiles and Space Co./LTV Aerospace Corporation, Dallas, Texas

A finite element method is used to determine the critical stress distribution in the canopy of a 4000 sq ft, twin keel, parawing with a 5000 lb payload. The analysis accounts for finite strains and nonlinear material properties, and includes both tape and anisotropic triangular membrane elements. The convergence of the finite element method is demonstrated by the results obtained for a tape-stiffened, cylindrical membrane using the parawing material properties and a uniform internal pressure distribution of the same mean intensity as that experienced by the parawing. Good convergence was not attained for the parawing solution due to the asymmetric geometry and loading conditions. However, the solution does predict failure stress levels in the region where a tear failure was experienced in the drop test. The results also imply that the use of additional suspension lines along the side lobe leading edges would reduce the fabric stress in the critical region.

Nomenclature

A	= surface area of membrane element, cross-sectional area of tape element
$[D]$	= matrix of stress-strain coefficients $\{\sigma\} = [D]\{\varepsilon\}$
D_{ij}	= components of $[D]$ in element coordinates
E	= elastic modulus for tape element
$[G]$	= stress-strain relations derived from test data $[D] = [G]^{-1}$
$[K]$	= system stiffness matrix
$[\hat{K}]$	= element stiffness matrix†
L	= length of tape element
l.e.	= wing leading edge
$L1, L2, \ldots, L6$	= leading-edge suspension lines,‡ left lobe
$R1, R2, \ldots, R6$	= leading-edge suspension lines,‡ right lobe
$LK1, \ldots, LK12$	= keel suspension lines,‡ left side
$RK1, \ldots, RK12$	= keel suspension lines,‡ right side
$LT1, LT2, LT3$	= trailing-edge suspension lines,‡ left side
$RT1, RT2, RT3$	= trailing -edge suspension lines,‡ right side
$\{P\}$	= system nodal load vector
$\{Q\}$	= system nodal displacement vector
t	= thickness of membrane
$\mathbf{u}$	= nodal displacement vector
u, v, w	= $x\ y\ z$ components of $\mathbf{u}$
x, y, z	= element coordinate system
x', y', z'	= lobe coordinate system
$E_w, E_f, G, \mu/E, \alpha, \beta$	= stress-strain coefficients for membrane element
$\{\varepsilon\}$	= element strain
$\varepsilon_x, \varepsilon_y, \gamma_{xy}$	= element strain components
$\{\sigma\}$	= element stress
$\sigma_x, \sigma_y, \tau_{xy}$	= element stress components
η, ξ, ζ	= generalized stresses, $\eta = \sigma_w t$, $\xi = \sigma_f t$, $\zeta = \tau_{wf} t$
θ_w	= angle from the x axis to the warp axis
$\Delta(\ )$	= increment in $(\ )$

Subscripts and Superscripts

i	= initial value for the current step
w, f	= warp and fill directions

Introduction

THE development of technology for flexible recovery devices having a capability for gliding flight has been pursued by the parawing research program at the NASA Langley Research Center for over a decade.[1,2] In the course of this work, difficulties were encountered with the deployment of the intermediate scale, twin keel, parawing. Repeated instances of canopy damage were experienced at intermediate dynamic pressures (60 psf). Drop tests and wind-tunnel experiments with smaller parawings had indicated that with proper reefing, dynamic pressures at deployment of 100 psf were feasible.[2-4]

In order to provide a better understanding of the parawing deployment problem, Langley Research Center considered it desirable to perform a structural analysis of the parawing canopy for one of the flights in which damage was experienced. As a prerequisite, a flight data analysis to determine the geometric, aerodynamic, and kinematic characteristics of the deployment phase of two representative drop tests was conducted for LRC by the Vought Missiles and Space Company.[5] In addition, an extensive test program to determine the coefficients describing the stress strain relations of the parawing fabric was undertaken by Langley Research Center.[6]

The purpose of this study is to determine the stress distribution in the canopy of the flight designated 203-T for the critical (failure) geometry and loading conditions obtained in Ref. 5, using the material properties defined in Ref. 6. A finite element method[7,8] is used. In view of the conditions implied by the material properties, geometry, and loading, the piecewise linear approach[9-11] was selected. The present application accounts for finite strains, nonlinear material properties, and includes both tape and anisotropic triangular membrane elements.

The results include the nodal displacements, reactions, and element stresses for each element of the entire right lobe of the parawing. These elements include the canopy membrane, seam reinforcement tapes, leading-edge tapes, and suspension lines. The basic equations and the essential details of the method of solution are also presented. The convergence of the method is demonstrated by the results obtained for a tape stiffened cylindrical membrane subjected to internal pressure.

Presented as Paper 70-1196 at the AIAA Aerodynamic Deceleration Systems Conference, Dayton, Ohio, September 14–16, 1970; submitted November 12, 1970; revision received September 21, 1971. This work was supported by the NASA Langley Research Center through Contract NAS1-6957. The author is indebted to R. B. Bost of V.M.S.C. for the matrix manipulation algorithms used in the development of the digital computer solution. The encouragement and helpful suggestions of V. L. Alley Jr. of the Langley Research Center are also gratefully acknowledged.

Index categories: Structural Static Analysis; Post-Entry Deceleration Systems and Flight Mechanics; Aircraft Deceleration Systems.

* Engineering Specialist, Loads and Dynamics Group, Structures and Materials Sec.

† The cap (ˆ) may be omitted where confusion with the system stiffness matrix is unlikely.

‡ Also used to denote the point at which the line is attached to the canopy.

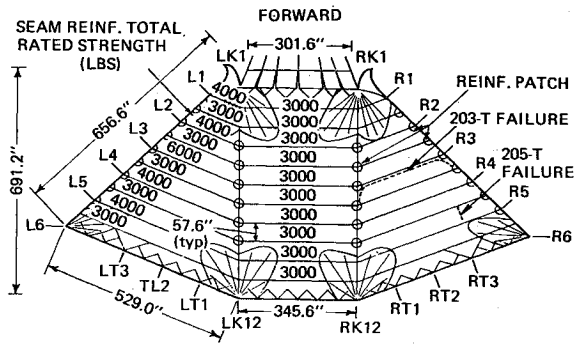

Fig. 1 Plan view of intermediate scale parawing.

Parawing Structure

The canopy structure and dimensions, together with the location and extent of the failure, is shown in Fig. 1. The canopy was fabricated from a low permeability (polyurethane coated) 2.25 oz/yd^2 nylon rip-stop fabric. The typical panel width was 28.8 in. Alternate panel seams were reinforced with nylon tapes (MIL-T-5608—1500 lb, 2000 lb, and 3000 lb rated strength) sewn on both top and bottom surfaces. The locations of particular tape types is indicated by the total rated strengths shown in Fig. 1. The keels and wing skirts were reinforced with nylon webbing (MIL-W-4088—3600 lb bottom side and 5500 lb top side for skirts; 9000 lb for keels, 2 per keel). Nylon cords (MIL-C-7515—3500 lb, 4500 lb, and 5500 lb, rated strength) were used for the suspension lines. Leading-edge suspension lines are designated $L1$, $L2$, ..., $L6$ and $R1$, ..., $R6$ for the left and right lobes, respectively. All are 5500 lb cords except for $R3$ and $L3$ which have a 10,000 lb rating. Trailing-edge suspension lines are designated $LT1$, $LT2$, $LT3$ and $RT1$, $RT2$, $RT3$ and all have a 3500 lb rating. Keel suspension lines (12 each side) were attached at the intersection of the seam reinforcement and the keel webbing. All are 4500 lb cords except for $LK1$, $LK12$, $RK1$, and $RK12$ which have a 5500 lb rating.

Geometry and Loading Conditions at the Critical Time

The parawing deployment process used in the tests consisted of four reefed stages followed by the fully inflated, gliding flight stage. The inflated shapes for the first four reefed stages are shown in Fig. 2. It was concluded in Ref. 5 that the critical loading conditions occurred during second stage reefed inflation. The first motion of the left lobe was observed immediately after the reefing lines were cut. Motion of the right lobe was observed 0.03 sec later, and the two lobes proceeded to inflate approximately simultaneously.

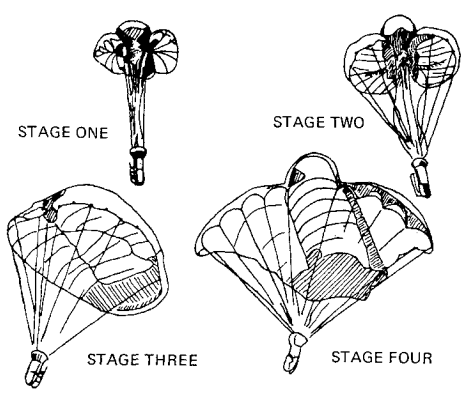

Fig. 2 Inflated canopy shapes.

At 0.21 sec after the first motion was observed the spanwise displacement of points $R3$ and $L3$ reached the maximum allowed by the canopy geometry and the spanwise motion was suddenly arrested. Simultaneously, a tear failure was observed in the right lobe near point $R3$, and the maximum suspension loads were recorded. Consequently, the conditions at this time were selected as the critical conditions for the right lobe.

The finite element model of the canopy is shown in Fig. 3. Figure 3a is a view of the elements of the upper surface of the right lobe, viewed from below. Similarly, Fig. 3b shows the elements of the lower surface. The circled numbers designate membrane elements. The numbers in parentheses refer to tape elements, and numbers at the intersections of the various elements are the node numbers. In all there are 81 nodes and 193 finite elements of which 130 are membrane elements. All of the nodes lie on the surface of the canopy, except for 80 and 81 which represent the right reel reef point and the suspension line attachment to the test vehicle, respectively. The x' y' z' axes shown form a right hand system with the z' axis positive downward. The position of each node relative to this system is given in Table 1.

Large pressure coefficients were identified in Ref. 5 as resulting from the arresting of flow by the sudden termination of the spanwise expansion of the lobes. These transient aerodynamics produced pressure differentials on the right lobe as high as six times the dynamic pressure of the freestream (8.0 psf). The critical aerodynamic loading is represented in Table 1 by the x', y' and z' force components at the node points.

In Ref. 5 the maximum decelerations were estimated as 193 g's for $R3$ and 109 g's for $L3$. Although these decelerations are quite large, the associated inertia loading is negligible compared with the aerodynamic loading because of the light weight of the canopy structure.

Method of Analysis

The linear incremental method employed herein is equivalent to an elementary scheme of forward integration with the generalized load, $\{P\}$, as the independent variable and the generalized displacement, $\{Q\}$, as the primary dependent variable. That is, let $\{\sigma_i\}^k$ and $\{\varepsilon_i\}^k$ denote the stresses and strains existing in element k at the beginning of the ith step, and let $[K(Q_i, \sigma_i)]$ and $[\hat{K}(Q_i, \sigma_i)]^k$ denote the corresponding system and element stiffness matrices. Then the incremental displacement, $\{\Delta Q_i\}$, resulting from the incremental load, $\{\Delta P_i\}$, is

$$[K(Q_i, \sigma_i)]^{-1}\{\Delta P_i\} = \{\Delta Q_i\} \tag{1}$$

The new total load and displacement are given by:

$$\{P_{i+1}\} = \{P_i\} + \{\Delta P_i\} \tag{2}$$

$$\{Q_{i+1}\} = \{Q_i\} + \{\Delta Q_i\} \tag{3}$$

and the new element strains and stresses are determined from:

$$\{\Delta\varepsilon_i\}^k = f^k(Q_i, \Delta Q_i) \tag{4}$$

$$\{\Delta\sigma_i\}^k = [\hat{K}(Q_i, \sigma_i)]^k\{\Delta\varepsilon_i\}^k \tag{5}$$

$$\{\sigma_{i+1}\}^k = \{\sigma_i\}^k + \{\Delta\sigma_i\}^k \tag{6}$$

where $\{\Delta\varepsilon_i\}^k$ and $\{\Delta\sigma_i\}^k$ are the increments in strain and stress of element k, corresponding to the incremental displacement, $\{\Delta Q_i\}$. These results are used to determine new element stiffness matrices, $[\hat{K}(Q_{i+1}, \sigma_{i+1})]^k$, from which the system stiffness matrix $[K(Q_{i+1}, \sigma_{i+1})]$, appropriate to the next load increment, $\{\Delta P_{i+1}\}$, is formulated. The process is then repeated with $\{\Delta P_{i+1}\}$, $\{\Delta P_{i+2}\}$, etc., until the desired loading, $\{P\} = \Sigma\{\Delta P_i\}$, is obtained.

Two types of finite element are employed: a tape (flexible rod) element and a membrane (flexible plate) element. Both

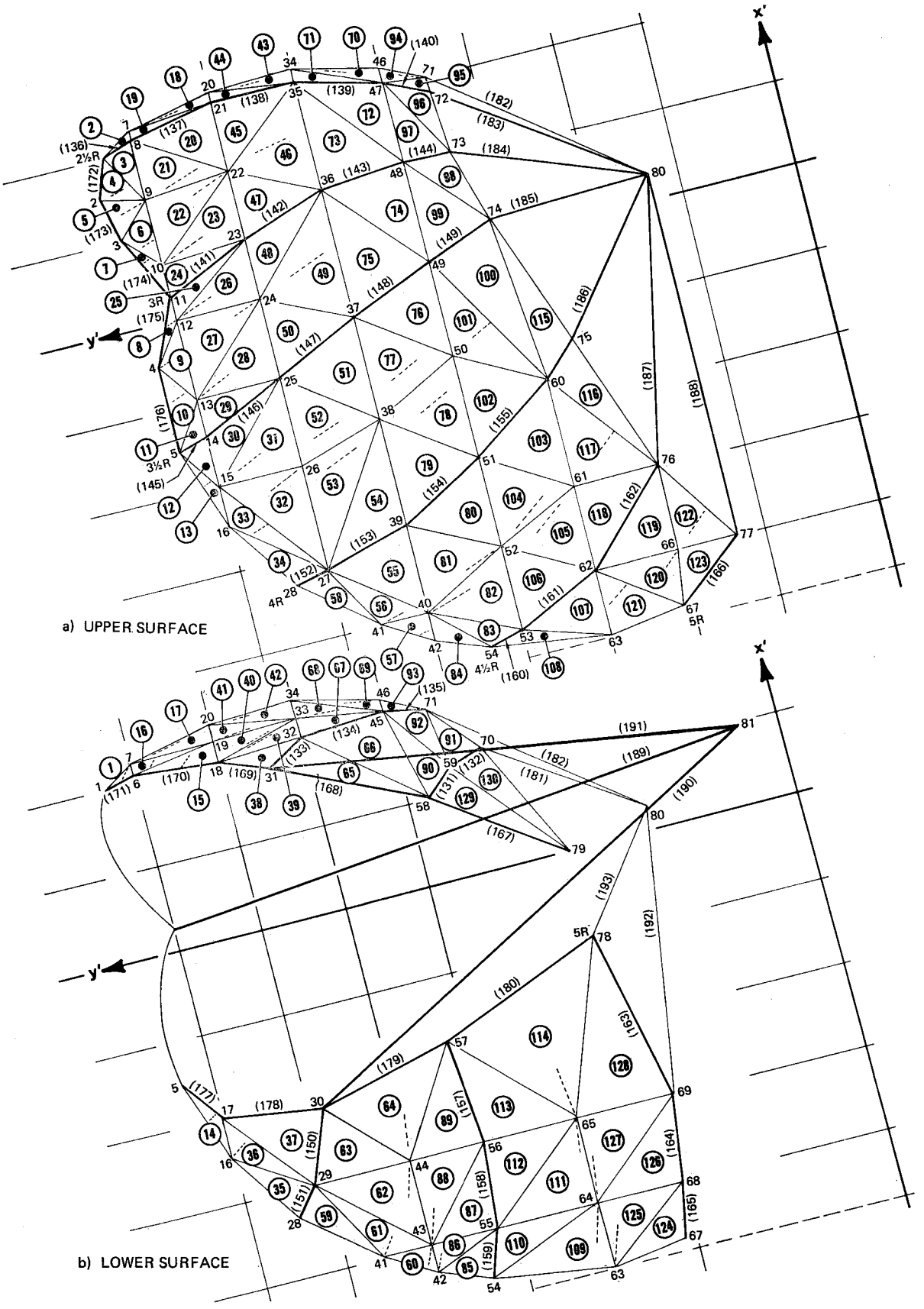

Fig. 3 Finite element model of parawing right-lobe.

Table 1 Coordinate locations and aerodynamic loading for parawing right lobe

Nd No	Coordinates, in.			Aerodynamic, load lb			Nd No	Coordinates, in.			Aerodynamic, load lb		
	x'	z'	z'	x'	y'	z'		x'	y'	z'	x'	y'	z'
1	59.4	233.2	−30.9	1.3	30.2	−33.8	42	−129.5	162.0	−9.6	−17.8	7.2	2.4
2	36.0	237.0	−22.5	−11.4	23.9	−27.8	43	−120.0	162.0	4.2	−17.3	6.2	19.5
3	30.0	233.8	−18.0	−26.6	55.2	−31.4	44	−90.0	162.0	26.2	−6.3	1.8	8.8
4	−15.0	232.3	−6.0	2.4	124.2	−42.6	45	63.0	132.0	−47.0	46.3	−13.8	45.8
5	−46.0	232.5	9.5	−27.2	118.6	−39.1	46	67.0	132.0	−54.5	28.5	−9.0	−6.5
6	62.5	222.0	−29.8	11.6	2.0	14.8	47	61.5	132.0	−62.2	62.5	−19.7	−81.3
7	66.4	222.0	−34.0	46.0	13.1	2.0	48	33.5	132.0	−78.0	59.6	−6.6	−150.0
8	63.1	222.0	−36.9	24.8	52.5	−89.6	49	−1.5	132.0	−87.0	21.5	10.0	−169.2
9	42.3	222.0	−38.0	−17.0	99.8	−120.3	50	−35.5	132.0	−85.0	−24.6	32.3	−114.0
10	19.5	222.0	−34.2	−68.9	102.8	−108.0	51	−71.8	132.0	−72.0	−47.4	44.1	−114.8
11	7.8	222.0	−11.2	−7.4	98.5	−45.6	52	−104.0	132.0	−56.2	−56.4	40.6	−85.8
12	0.0	222.0	−29.3	51.9	177.6	−115.8	53	−133.7	132.0	−29.5	−47.5	18.7	−38.3
13	−28.5	222.0	−28.8	−35.3	201.5	−141.8	54	136.5	144.0	−11.8	−29.9	8.2	0.9
14	−42.6	222.0	−14.1	−25.0	78.2	−52.1	55	−120.0	138.0	9.5	−12.6	3.6	13.5
15	−60.0	222.0	−13.7	−42.3	135.8	−88.8	56	−90.0	135.5	27.5	−6.1	1.6	9.5
16	−75.0	222.0	3.5	−29.4	55.1	−8.9	57	−53.2	139.2	53.5	−0.3	0	0.7
17	−60.0	222.0	20.7	−7.4	10.7	7.1	58	30.0	124.0	−24.5	22.4	−3.3	30.8
18	60.0	192.0	−27.4	8.5	−3.4	16.9	59	38.8	114.2	−29.0	20.3	0.3	22.9
19	67.5	192.0	−31.0	41.8	−1.4	32.1	60	−52.0	102.0	−87.0	−6.0	−12.2	−135.7
20	73.1	192.0	−42.6	72.8	7.2	1.3	61	−90.0	102.0	−76.0	−31.9	19.2	−73.8
21	69.4	192.0	−48.7	55.8	38.2	−89.2	62	−120.0	102.0	−57.5	−59.7	13.1	−62.0
22	45.0	192.0	−59.0	23.6	12.5	−242.3	63	−143.0	102.0	−24.0	−38.5	1.9	−9.4
23	20.7	192.0	−52.5	−4.9	138.2	−162.7	64	−120.0	102.0	19.0	−12.1	1.0	8.6
24	0.0	192.0	−57.6	18.7	180.5	−219.7	65	−90.0	102.0	38.5	−1.9	0.7	3.5
25	−30.0	192.0	−57.0	−40.6	156.3	−175.7	66	−120.0	72.0	−60.0	−26.9	−7.7	−23.4
26	−60.0	192.0	−47.4	−52.6	75.5	−90.9	67	−139.0	75.4	−20.0	−28.1	−4.8	−11.8
27	−98.0	192.0	−14.8	−81.6	98.3	−103.0	68	−120.0	72.0	23.0	−6.1	0	3.5
28	−100.0	203.5	1.2	−14.7	16.0	−1.8	69	−90.0	68.0	43.0	−1.1	0.3	2.0
29	−90.0	195.6	15.6	−18.1	12.9	19.6	70	42.9	102.0	−28.2	6.7	2.8	7.7
30	−60.0	185.7	32.4	−0.5	0.4	1.3	71	60.0	117.5	−53.5	25.5	−9.4	3.9
31	54.0	175.0	−30.0	4.1	−1.6	5.3	72	54.6	117.5	−62.0	9.1	−4.5	−13.7
32	61.2	162.0	−39.4	21.0	−7.4	30.3	73	32.7	115.5	−70.0	17.4	−15.5	−36.7
33	68.1	162.0	−43.2	38.5	−10.8	33.1	74	7.0	107.8	−77.0	19.5	−31.2	−77.5
34	74.4	162.0	−52.2	58.7	−6.9	−7.0	75	−40.0	90.5	−77.5	6.3	−15.9	−27.1
35	69.0	162.0	−58.4	91.0	33.4	−167.7	76	−90.0	72.0	−78.5	−17.8	−10.5	−56.1
36	30.0	162.0	−73.2	46.0	110.4	−258.3	77	−120.0	51.0	−40.6	−11.4	−8.9	−9.6
37	−15.3	162.0	−78.3	−6.8	95.4	−191.7	78	−30.0	81.2	38.5	0	0	0.5
38	−50.7	162.0	−68.7	−70.0	87.3	−160.3	79	0	81.2	6.5	0	0	0
39	−88.2	162.0	−49.4	−50.9	62.5	−91.3	80	9.0	51.0	0	0	0	0
40	−120.0	162.0	−28.7	−53.7	43.9	−57.7	81	28.0	12.0	520.0	0	0	0
41	−120.0	178.8	−7.6	−23.6	19.0	−3.7							

types have three translational degrees of freedom per node and derive their resistance to differential transverse nodal displacements during a particular step from the tension in the element at the beginning of the step. The transverse displacements referred to are the (nonrigid) out of plane nodal displacement for the membrane and the component of the resultant relative displacement of the ends of the tape element which is normal to the axis of the element. This initial stress stiffness is coupled with the conventional stiffness through the definition of the strain energy and the adoption of a nonlinear definition of strain (i.e., through geometric nonlinearity).

In the linear-incremental procedure outlined above, the geometry is updated at the end of each step and the element stiffness matrices are defined for the new geometry and the accumulated stress levels. Also, a new load increment which accounts for the dependence of loading on geometry, is defined.

Several other piece-wise linear approaches were used in the analysis. However, each of these is a special case of the general procedure, obtained by placing restrictions on the definitions of some of the terms entering Eqs. (1–6). The variations employed were: (a) constant load increment, i.e., the load increment does not vary with the geometry. (b) Constant reference geometry—here the load increment is constant in the sense of (a), and element stiffness matrices vary only with the accumulated stress. (c) Iteration—if iteration is required for the $i+1$st step, the load increment, $\{\Delta P_i\}$, and the accumulated stresses and displacements, σ_i, $\{Q_i\}$, are taken as constant reference values. The element stiffness matrices vary only with the stress increments, e.g., for the nth iteration of the simplest type,

$$[\hat{K}] = [\hat{K}(Q_i, \sigma_i + \tfrac{1}{2}\Delta\sigma_{n-1})] \tag{7}$$

Convergence is obtained if $\Delta\sigma_n - \Delta\sigma_{n-1} \to 0$.

Material Properties

The difficulties associated with any geometrically nonlinear problem are compounded in the analysis of flexible deceleration systems by the character of the materials normally used in their manufacture. In particular, it was found in Ref. 6 that the nylon fabric used in manufacturing the parawing canopy is completely anisotropic. That is, nine independent coefficients are required in the planar stress-strain relations of a membrane element. Moreover, the coefficients were found to be nonlinear functions of the state of stress. In the piecewise linear method of analysis, as in the classical linear theory of elasticity, the existence of the strain energy density function necessary for the development of the theory requires that the matrix of elastic coefficients for the membrane elements be symmetric. For this reason, symmetry was enforced by an averaging process. The result is an approximation of the material behavior by six independent coefficients rather than nine.

The nonlinearity of the stress-strain relations can be accounted for at the beginning of each step by merely redefining the elastic constants in the formulation of the element stiffness matrices, $[\hat{K}(Q_i, \sigma_i)]$. However since the canopy material is anisotropic, the stress-strain coefficients for the membrane elements are known functions of stress only for the coordinate axes used in the material tests. It is necessary, therefore, to determine at each step in the solution the orientation of the test directions in an individual membrane element relative to the element coordinate system defined for its current configuration.

In the undeformed state, these test directions are referred to as the warp and fill directions. The parawing was fabricated with the warp direction parallel to the reinforcement tapes, (Fig. 1). However, not all of the membrane elements in the finite element model (Fig. 3) are bounded by a reinforcement tape. The assumed initial warp direction for such elements is designated by a broken line in Fig. 3.

The averaged (symmetrized) test data yield stress-strain relations of the form $\{\varepsilon\} = [G]\{\sigma\}$ where $[G]$ is the symmetric stress-strain coefficient matrix. Relative to the test directions (warp and fill), these relations are given as:

$$\begin{Bmatrix} \varepsilon_w \\ \varepsilon_f \\ \gamma_{wf} \end{Bmatrix} = \begin{bmatrix} \frac{1}{E_w t} & -\frac{\mu}{Et} & \frac{\alpha}{t} \\ & \frac{1}{E_f t} & \frac{\beta}{t} \\ \text{Sym} & & \frac{1}{Gt} \end{bmatrix} \begin{Bmatrix} \sigma_w t \\ \sigma_f t \\ \tau_{wf} t \end{Bmatrix} \tag{8}$$

where the six independent coefficients are functions of the stresses $\sigma_w t$, $\sigma_f t$, $\tau_{wf} t$ and t represents the (hypothetical) thickness of the membrane.

Since each of the stress-strain coefficients is a function of the state of stress, the analysis can be simplified by an explicit approximation of this functional dependence. In particular, a quartic surface in the three stresses ($\eta = \sigma_w t$, $\xi = \sigma_f t$, $\zeta = \tau_{wf} t$) was fitted to the $E_w t$, $E_f t$ test data of Ref. 6 and the averaged $1/G$, α/t and β/t data. A cubic surface in η and ξ was fitted to the averaged values of μ/Et. (The $(\mu/Et)_w$ and $(\mu/Et)_f$ data are assumed independent of the shearing stress.) The general quartic in η, ξ, ζ is

$$\begin{aligned} F = {} & a_1 + a_2\eta + a_3\xi + a_4\zeta + a_5\eta^2 + a_6\eta\xi + a_7\eta\zeta + \\ & a_8\xi^2 + a_9\xi\zeta + a_{10}\zeta^2 + a_{11}\eta^3 + a_{12}\eta^2\xi + \\ & a_{13}\eta^2\zeta + a_{14}\eta\xi^2 + a_{15}\eta\xi\zeta + a_{16}\eta\zeta^2 + a_{17}\xi^3 + \\ & a_{18}\xi^2\zeta + a_{19}\xi\zeta^2 + a_{20}\zeta^3 + a_{21}\eta^4 + a_{22}\eta^3\xi + \\ & a_{23}\eta^3\zeta + a_{24}\eta^2\xi^2 + a_{25}\eta^2\xi\zeta + a_{26}\eta^2\zeta^2 + \\ & a_{27}\eta\xi^3 + a_{28}\eta\xi^2\zeta + a_{29}\eta\xi\zeta^2 + a_{30}\eta\zeta^3 + a_{31}\xi^4 + \\ & a_{32}\xi^3\zeta + a_{33}\xi^2\zeta^2 + a_{34}\xi\zeta^3 + a_{35}\zeta^4 \end{aligned} \tag{9}$$

The expansion coefficients a_i relative to the general quartic, are presented in Table 2 for each of the stress-strain moduli. The null coefficients reflect the order of the fit in a given stress. In particular, during the testing[6] of a warp specimen, data were obtained for $E_w t$ vs η curves at five or more values of η and ζ but at only three values of ξ. Thus, a quadratic is the highest order fit permissible in the fill direction, and any term containing powers of ξ greater than the second must be deleted prior to fitting the data. Similarly, powers higher

Table 2 Quartic expansion coefficients for membrane stress-strain relations[a]

Coef. No.	Stress-strain coefficient					
	$E_w t$	$E_f t$	Gt	μ/Et	α/t	β/t
1	.37820E+3	.24074E+3	.55354E+1	.60800E−3	−.12834E−2	−.24446E−2
2	.52486E+1	−.93098E+1	.58036E−1	−.11017E−4	.30310E−3	.43471E−3
3	.35934E+1	−.19504	.58310E−1	−.10710E−4	.18922E−3	.24651E−3
4	.68208E+3	.27017E+3	−.26130E+2	0.0	−.12876E−4	−.83920E−2
5	.60897E−1	.16208	−.16794E−1	.14558E−6	−.16399E−4	−.13816E−4
6	−.20957E−2	.12605	.49002E−1	.14837E−7	−.30787E−4	−.43068E−4
7	−.35201E+1	.12651E+2	.75753	0.0	.68016E−3	.18114E−4
8	−.66092E−1	.23901	−.16876E−1	.13983E−6	−.55952E−5	−4.2732E−5
9	−.20916E+2	−.29007E+1	.75895	0.0	.48865E−4	.29935E−3
10	−.31377E+3	−.12629E+3	.54675E+2	0.0	.30918E−2	.23848E−2
11	.18112E−2	0.0	.12673E−2	−.63958E−9	.28777E−6	0.0
12	.43526E−2	−.39288E−2	−.21829E−2	−.74981E−10	.13536E−5	.13168E−5
13	.45748E−1	−.15018	−.57274E−2	0.0	−.11560E−4	.12046E−4
14	.35527E−2	.17024E−2	−.21755E−2	−.55673E−10	.44784E−6	.85938E−6
15	−.88050E−1	.44563	.42006E−1	0.0	−.18613E−5	.60596E−5
16	.11019E+1	−.15404E−2	−.97909E−1	0.0	−.90790E−4	−.17214E−3
17	0.0	−.31879E−2	.12700E−2	−.61285E−9	0.0	−.64859E−7
18	.48314	−.79805E−2	−.57924E−2	0.0	.50989E−5	−.51281E−5
19	.11529E+2	.16541E+1	−.97919E−1	0.0	−.25707E−4	−.17304E−4
20	−.36975E+1	.34163E+2	−.31253E+2	0.0	−.78957E−3	−.33674E−3
21	−.28222E−4	0.0	−.17915E−4	0.0	−.13579E−8	0.0
22	−.22040E−4	0.0	.37916E−4	0.0	−.16708E−7	0.0
23	−.13031E−3	0.0	.15169E−3	0.0	.51162E−7	0.0
24	−.72831E−4	−.19664E−5	−.45126E−6	0.0	−.88668E−8	−.24285E−7
25	−.74450E−3	−.34369E−2	−.53828E−3	0.0	−.74068E−7	−.35342E−6
26	−.16779E−2	.12922	.58429E−3	0.0	.10816E−5	−.11477E−5
27	0.0	−.92760E−5	.37787E−4	0.0	0.0	−.11758E−8
28	−.12962E−2	.35002E−4	−.53807E−3	0.0	−.15361E−6	−.86555E−7
29	−.58793E−1	−.91519E−1	.25824E−2	0.0	.25194E−5	.22943E−5
30	−.37215	.26141E+1	−.55272E−1	0.0	.34944E−5	.27762E−4
31	0.0	.14123E−4	−.17935E−4	0.0	0.0	.14521E−8
32	0.0	−.35774E−3	.15193E−3	0.0	0.0	.38235E−7
33	−.21072	.17502E−1	.59921E−3	0.0	−.21616E−6	−.88832E−7
34	.10011	−.40235	−.55379E−1	0.0	−.59589E−5	−.10651E−5
35	.73698E+1	−.37886E+1	.53358E+1	0.0	.95031E−4	−.81718E−5

[a] the notation $aE + b$ means $(a) \times (10^{+b})$

Table 3 Elastic properties of tape elements

Parawing element no.	Modulus EA (lb)
131, 132, 136–140, 145–149, 157–162, 181, 183, 185, 187	5,600
133, 134, 135, 150–156, 163–166, 182, 186, 188	11,400
141–144, 184	22,000
167–180, 192, 193	32,200
189	20,000
190, 191	7,200

than the second in η had to be deleted prior to fitting the $E_f t$ data. Finally, the zero coefficients for μ/Et follow from the use of a cubic in η and ξ and the fact that μ/Et was assumed independent of ζ.

The coefficients shown in Table 3 represent test data for shear stresses in the range $-3.0 \leq \zeta \leq 3.0$ lb/in., and for ξ and η up to about 25 lb/in. That is, the warp specimens were tested in the warp direction for stresses exceeding 50 lb/in. but only up to 25 lb/in. in the fill direction. A similar statement holds for the fill specimens. The range of the coefficients was extended to approximately 50 lb/in. in η and ξ by fitting a combination of test points and extrapolated points. In the analysis, if the stress in an element exceeded the range of validity, the stress-strain coefficients were evaluated at the range limit, i.e., 50 lb/in.

It is important to note that the membrane elements cannot support compression. If a solution indicates that compressive stress, say $\xi = -5.0$ lb/in., exists in an element, the moduli for the next step are evaluated for $\xi = +1.0$ lb/in. and η and ζ equal to the actual values. Negative shear stress is possible, and the shear modulus G is an even function of ζ. On the other hand, α and β, the coefficients of interaction of the first and second kinds,[12] are odd functions of ζ.

The suspension lines and reinforcement tapes are represented by tape elements. Test results indicate a linear range for these elements which includes the expected loading for the problems considered here. For this reason, the elastic moduli for the tape elements were assumed to be constant. The values used are given in Table 3.

The element stiffness matrices used in the analysis were derived following Ref. 9. (An alternative derivation is presented in Ref. 11.) The tape element stiffness matrix is in agreement with Eq. (11),[9] and the geometrical stiffness for the membrane element is a generalization of Eq. (37)[9] to include anisotropic material properties. The current membrane element stiffness matrix (element coordinates) is given by Eq. (10). The numbers u_i, v_i, w_i are the x, y, z (element axis) coordinates of the displacements of node i. The origin of the element coordinate system is at node 1. Nodes 2 and 3 have coordinates $(x_2, 0, 0)$ and $(x_3, y_3, 0)$ respectively. The parameters a and b are defined as

$$a = (x_3 - x_2)/x_2 y_2, \quad b = x_3/x_2 y_2$$

and $\tau = \tau_{xy}$. The superscript i has been dropped from the initial stress, A denotes the surface area of the triangle, and D_i are the elements of the matrix, $[D]$, of stress strain relations $D_1 = D_{11}$, $D_2 = D_{22}$, $D_3 = D_{33}$, $D_4 = D_{12}$, $D_5 = D_{13}$, $D_6 = D_{23}$, the matrix $[D]$ is obtained by transforming the square matrix of Eq. (8) to element coordinates and inverting.

$$\frac{1}{tA}[\hat{K}] =$$

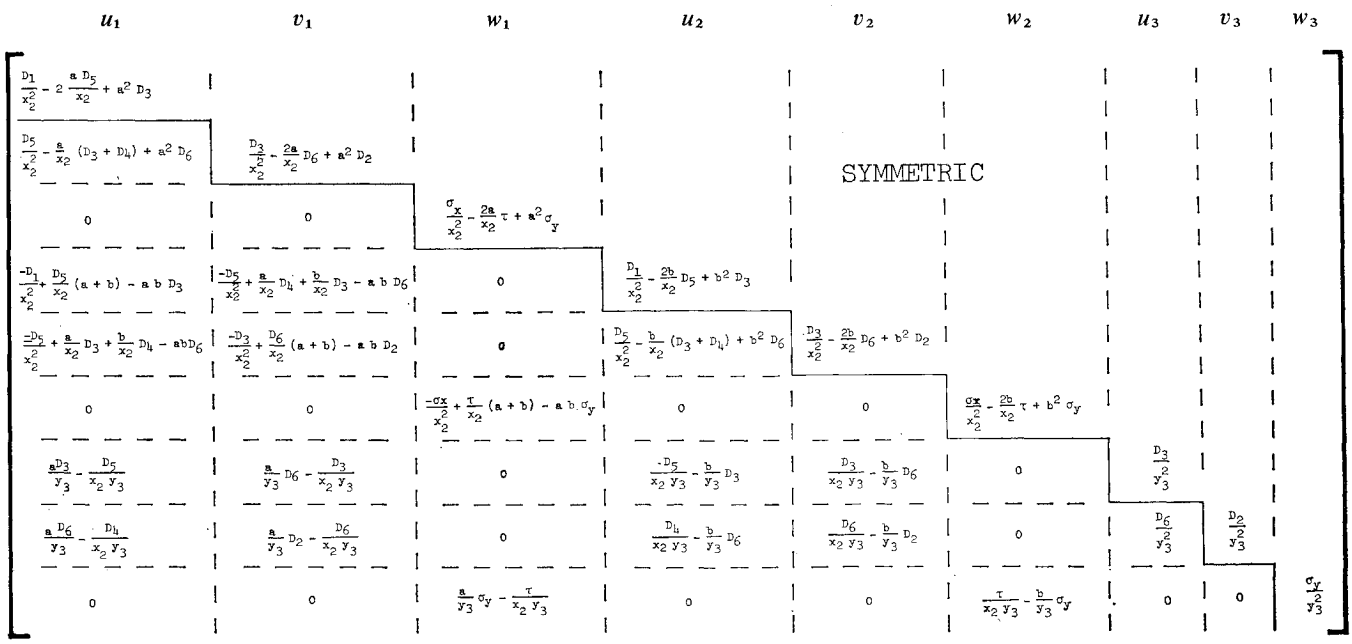

(10)

Test Problem, Results and Discussion

In order to demonstrate the convergence of the finite element method, several solutions were obtained for a tape-stiffened cylindrical membrane subjected to a uniform internal pressure. To obtain a degree of similarity to the parawing, an undeformed radius of 10.0 ft was selected, the parawing material properties were used, and the internal pressure was taken as the mean intensity experienced by the parawing in the regions of primary interest. The plan view of the finite element model is shown in Fig. 4. The numbers at the intersections of the elements are node numbers. The circled numbers designate membrane elements. Tape elements connect nodes 1, 2...7 and 29, 30...35. These tape elements all have an elastic modulus of $EA = 8340$ lb. In all there are 35 nodes and 60 elements of which 48 are membrane elements. The free-free system has 105 degrees of freedom. Of these, 24 are constrained by the boundary conditions, resulting in

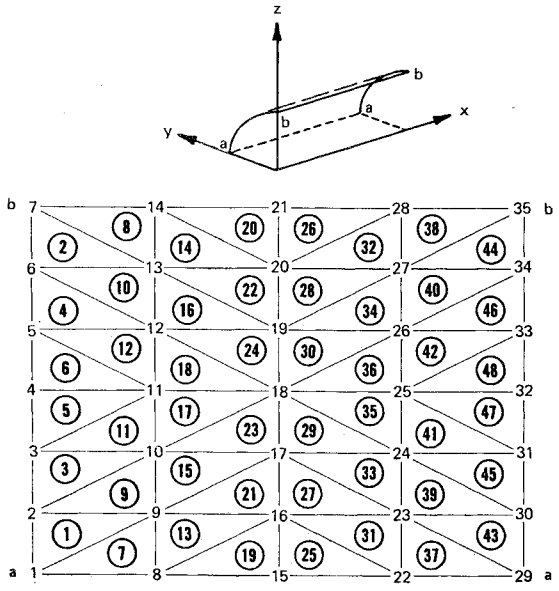

Fig. 4 Test problem elements, plan view.

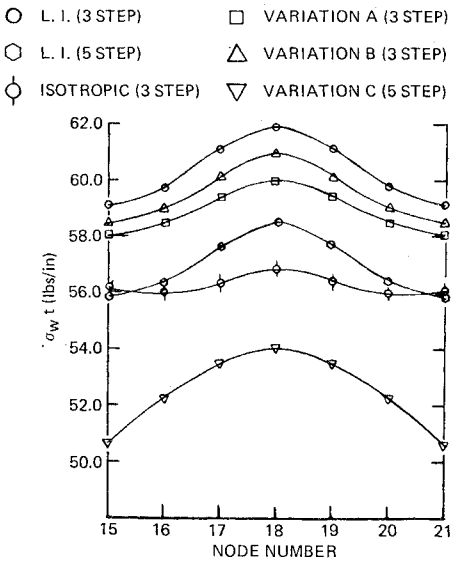

Fig. 5 Warp stress along node line 15–21 for test problem.

81 degrees of freedom for the constrained system. Referring to Fig. 4, the cylinder is restrained against longitudinal x displacement at its ends, and against tangential displacements along sides a and b. The warp direction parallel to 1–7.

The most important problem associated with applying the piecewise linear method to an initially unstressed tension structure is the determination of the proper element stress level to be used with the first load increment. It was found that an iteration process is required to determine the state of initial stress (in each element) which insures a correct start on the solution. A three-cycle process was used for the cylinder problem. For the first cycle, an estimate is made of the minimum stress that could exist in an element in equilibrium with the prescribed load increment. The initial state of stress for the element is then taken as an order of magnitude larger than the minimum. Shearing stresses are assumed to be zero. For example, for a tape element with length L (in.) and an incremental distributed load Δw (lb/in.), the minimum stress is $\sigma A = \Delta w\, L/2$ (lb), corresponding to a completely slack configuration. Thus, the initial stress is taken as $\sigma_1 A = 5.0 \Delta w L$. Similarly, for a triangular membrane element of base length x_2 and altitude y_3, with an incremental distributed load ΔW (lb/in.^{2}), the initial stress is taken as

$$\sigma_x t = \sigma_y t = 5.0 \Delta W\, x_2 y_3/(x_2 + y_3),\ \tau_{xy} = 0$$

After defining the initial stresses, $\{\sigma_1\}^k$, the element and system stiffness matrices corresponding to these stresses and the initial configuration, $\{Q_1\} = \{0\}$, are formed. An increment in stress, $\{\Delta\sigma\}^k$, is obtained by applying the first load increment, $\{\Delta P_1\}$, and solving equations 1, 4 and 6. A new initial stress is then defined as $\{\sigma_1\}^k = \frac{1}{2}\{\Delta\sigma_1\}^k$, and the process is repeated. Three cycles were sufficient to insure convergence of the $\{\sigma_1\}^k$ to within 10%. This iteration is identical to that described by Eq. (7) with the unstressed state as the reference configuration.

Using the starting values as outlined above, six solutions to the cylinder problem were obtained. These include 3-step and 5-step linear-incremental (l.i.) solutions, a 3-step piecewise linear solution with constant load (variation A), a 3-step piecewise linear solution with constant geometry (variation B), and an iterative solution (variation C). With one exception, the solutions employed parawing material properties. The exception was a three step l.i. solution where constant isotropic coefficients corresponding to the unstressed parawing values for E_w, G, and μ/E, were used.

The distribution of warp stress along the line connecting nodes 15–21 is presented in Fig. 5 for each of the six solutions. It is interesting to note that of the 3-step solutions using parawing material properties, the linear incremental solution predicts the largest stresses and the constant load increment (variation A) predicts the lowest. This is to be expected, since the linear-incremental solution accounts for the changes in geometry in both the element stiffness definition and in the determination of the load increment (from a prescribed constant pressure increment), while the constant load increment solution applies the same nodal loading at each step to a deformed configuration which, in effect, reduces the applied pressure increment.

The itotropic 3-step l.i. solution predicts a maximum warp stress which is 8% less than the maximum predicted by the same type of solution using parawing material properties. On the other hand, the maximum fill stress in the isotropic solution was approximately 17 lb/in. compared with 6 lb/in. for the parawing material. This increase in biaxial coupling is in keeping with the increase in the modulus of elasticity in the fill direction to a value equal to the warp modulus.

The 5-step l.i. solution predicts a maximum warp stress which is 5% less than the maximum predicted by the comparable 3-step l.i. solution, indicating convergence from above. This is a logical result of the membrane element formulation, since the resistance to differential transverse displacements of an element under the action of a load increment is developed entirely by the stress in the element at the time the increment is applied. Thus, starting from a given state of stress, a load increment applied in one step will (for stable structures) yield larger displacements and final stresses than would result if the same load increment were applied in several steps with a redefinition of element stress (and hence stiffness) at the beginning of each step.

The iterative solution (variation C) represented in Fig. 5 was obtained by executing five iterations with the total load. Element stiffnesses were redefined at the beginning of each step according to Eq. (7), with the unstressed geometry being used as the reference configuration. The initial stresses were estimated by the same technique employed for the incremental solutions, with the total load used in the place of the load increment. It is noteworthy that the iterative solution predicts a maximum warp stress which is 14% less than that predicted by the 3-step l.i. solution. This result seems to contradict the sense of convergence implied by the 3-step and 5-step l.i. solutions. Such a judgement is premature, however, since the history of the elastic moduli as functions of stress as used in the l.i. solutions approximates the prescribed stress-strain relations whereas in the iterative solution, the final

stress (σ) is based only on material properties appropriate to $\sigma/2$. Furthermore, the iterative solution is based on a constant reference geometry which, (as noted above) naturally leads to a lower estimate of stress than would be predicted by a comparable l.i. solution.

Parawing Solution

The boundary conditions for the parawing problem were selected to represent the flight conditions as nearly as possible. In particular, the only constrained degrees of freedom are those at nodes 79–81, so that, in effect, the parawing lobe is free except for the restraints at the center lobe reef point and the suspension line attach point to the test vehicle. The result is a 234 degree-of-freedom representation.

Solutions for the parawing proved to be much more difficult to obtain than was expected based on the success of the test problem. Indeed, the degree of convergence of the first step, necessary to support a linear incremental solution, (or variations *A* or *B*), was never achieved. As a last resort, a 1-step iterative solution was attempted. That is, the entire load of Table 1 was applied at each iteration. After twenty iterations, the solution trend was established to the extent that average results can be presented with a reasonable degree of confidence. These results are shown in Tables 4–6, and in Fig. 6. Table 4a presents the membrane stresses, while Table 4b gives the stresses in the tape elements. The reactions at the constraints are presented in Table 5, and the average nodal displacements are given in Table 6. Finally, Fig. 6 shows the stress distribution in the region where the canopy failure was experienced.

Based on their variations in the final iterations, the nonzero stresses shown in Fig. 6 should be within 20 lb/in. of their final values. Since the fabric breaking strengths are approximately 100 lb/in. in warp and 85 lb/in. in fill, these results predict a failure in the region where the failure actually occurred. Furthermore, based on the results of the test problem, the stresses predicted by the iterative solution should be smaller than those predicted by a linear incremental solution. It seems likely, therefore, that the canopy failure was due to the severity of the loading rather than an initial weakness in the fabric. The process of convergence (i.e., the intermediate solutions) indicated that the probable reason for the high loading in the region of failure was the absence of a suspension line at $R3\frac{1}{2}$ (Fig. 1). It was found that the stress in the fabric between *R*3 and *R*4 is reduced considerably if a larger axial load (i.e., transverse stiffness) is carried by tape $R3\frac{1}{2}$. This would be the case if $R3\frac{1}{2}$ terminated in a suspension line.

The large number of iterations required in the solution was necessitated by the tendency of certain elements to go into compression. This tendency is the result of the asymmetric

Table 4a Element stresses for parawing; membrane element stresses (lb/in.)

Element No.	$\sigma_w t$	$\sigma_f t$	$\tau_{wf} t$	Element No.	$\sigma_w t$	$\sigma_f t$	$\tau_{wf} t$	Element No.	$\sigma_w t$	$\sigma_f t$	$\tau_{wf} t$
1	...	30	6	44	...	5	10	87	...	7	....
2	86	136	−36	45	10	27	2	88	...	...	....
3	...	...	....	46	44	13	8	89	1	1	....
4	115	71	−34	47	...	...	....	90	4	...	33
5	...	...	....	48	23	8	7	91	670	660	75
6	...	10	15	49	88	25	−5	92	31	19	4
7	...	...	....	50	85	25	2	93	...	...	....
8	90	79	16	51	11	25	10	94	102	26	8
9	115	85	16	52	5	36	2	95	48	35	11
10	...	...	....	53	28	5	−4	96	66	22	6
11	54	29	11	54	7	8	−4	97	36	8	....
12	53	37	5	55	...	2	1	98	48	13	11
13	95	24	−14	56	1	12	1	99	46	1	1
14	105	7	−31	57	...	...	....	100	42	...	−1
15	70	66	−8	58	...	...	....	101	36	7	6
16	...	60	−12	59	...	6	....	102	44	15	− 9
17	120	105	30	60	1	6	1	103	35	5	−3
18	...	42	−23	61	...	3	−4	104	30	6	1
19	48	...	44	62	12	1	1	105	20	3	....
20	...	17	−13	63	10	2	0	106	2	2	....
21	120	35	26	64	4	...	0	107	5	9	....
22	...	56	21	65	2	26	−6	108	...	4	−1
23	...	47	21	66	6	16	−1	109	2	1	....
24	78	60	20	67	6	43	1	110	7	...	....
25	...	107	−4	68	170	130	−70	111	22	13	−10
26	16	...	−7	69	225	245	−80	112	...	1	....
27	...	207	29	70	35	150	14	113	1	1	....
28	...	6	8	71	...	720	−345	114	5	8	−4
29	43	89	25	72	60	26	1	115	22	60	−5
30	29	30	−3	73	48	12	9	116	29	...	....
31	...	15	10	74	60	21	15	117	38	12	−10
32	35	26	−10	75	67	5	4	118	14	1	....
33	46	26	−2	76	48	12	−8	119	17	...	....
34	18	11	1	77	56	23	−8	120	...	20	−6
35	53	33	−18	78	40	10	−7	121	8	...	−3
36	...	...	....	79	85	28	16	122	5	3	....
37	95	48	−26	80	...	1	−2	123	32	10	−3
38	27	56	4	81	4	6	0	124	1	1	....
39	27	38	4	82	5	6	0	125	2	6	−3
40	22	23	2	83	18	9	−1	126	4	...	....
41	61	...	−55	84	3	15	−5	127	...	15	....
42	...	...	....	85	6	1	0	128	...	12	3
43	96	14	4	86	7	...	−1	129	58	52	−12
								130	4	...	−1

Table 4b Element stresses for parawing; tape element stresses

El. no.	σ_A (Lb)	El. no.	σ_A (Lb)	El. no.	σ_A (Lb)
131	58	152	382	173	4030
132	162	153	440	174	720
133	630	154	537	175	2145
134	364	155	626	176	2230
135	464	156	629	177	2505
136	...	157	8	178	1498
137	40	158	...	179	334
138	77	159	83	180	530
139	566	160	231	181	125
140	338	161	56	182	140
141	735	162	173	183	167
142	1705	163	146	184	1369
143	1400	164	162	185	835
144	1305	165	69	186	1100
145	250	166	409	187	407
146	288	167	655	188	308
147	547	168	1560	189	1105
148	424	169	1765	190	480
149	325	170	1050	191	178
150	173	171	1780	192	829
151	138	172	1805	193	1350

character of the geometry and loading. Since the structure cannot actually support such a state, the compressive stress must be ignored in the formulation of the element stiffness matrices. This results in an erratic pattern of stiffness definition and hence, the procedure is not actually an iteration process. It is more accurately characterized as a search for a tension state. It was found that the simple process given by Eq. 7 is not adequate for such a search, since it tends to diverge once an element has gone into compression. However, a modification of the process obtained by averaging the increments improved the stability. Explicitly, for the nth iteration (from the unstressed state),

$$[\hat{K}] = [\hat{K}(\tfrac{1}{4}(\Delta\sigma_{n-2} + \Delta\sigma_{n-1}))]$$

Furthermore, the automatic process for selecting an initial tension in the elements (described in the preceding section) tends to underestimate the loads carried by the tape elements. This leads to an initial divergence of the parawing solution, since the tension in the tape elements furnishes nearly all of the restraint against large displacements of the system as a whole. On the other hand, up to the iteration at which

Table 5 Reactions at parawing constraints

Node no.	Force component (lbs) x'	y'	z'
79	−365	− 585	398
80	591	−1202	2346
81	− 33	− 447	1166

Table 6 Parawing nodal displacements

Node No.	Displacement comp. in. x'	y'	z'	Node No.	Displacement comp, in. x'	y'	z'
1	4.5	+4.0	−14.3	40	−4.9	9.7	−28.4
2	2.0	−3.6	−21.6	41	2.0	8.6	−27.6
3	2.7	−1.6	−18.8	42	0.4	9.2	−26.3
4	5.0	7.7	−23.9	43	−0.3	9.6	−25.8
5	0.0	6.4	−29.5	44	−3.2	10.2	−21.8
6	2.5	3.3	−13.1	45	−3.5	−1.1	−5.5
7	3.5	0.7	−12.7	46	−4.0	2.3	−0.2
8	3.3	3.8	−11.2	47	−4.6	2.8	−1.8
9	6.5	−0.6	−15.3	48	−0.6	−0.3	−9.6
10	6.5	−0.6	−25.5	49	1.5	0.8	−19.2
11	1.2	−0.3	−23.8	50	1.9	2.6	−18.3
12	−6.5	−3.3	−23.1	51	−0.7	4.2	−22.7
13	5.0	4.0	−57.1	52	−2.0	7.2	−25.8
14	3.5	12.5	−39.3	53	−3.6	7.5	−23.8
15	3.5	6.9	−28.1	54	−5.5	9.2	−24.2
16	0.7	8.9	−29.1	55	−0.7	9.8	−22.6
17	−3.1	7.2	−33.5	56	−0.9	9.9	−22.7
18	−0.5	2.5	−14.9	57	−3.1	11.6	−20.0
19	−1.8	3.1	−17.9	58	0.0	1.5	−0.4
20	−5.5	10.3	−13.4	59	0.3	1.8	−0.1
21	−4.7	5.6	−16.5	60	3.2	1.5	−12.2
22	−5.0	4.2	−18.7	61	0.1	4.3	−17.5
23	−7.0	8.0	−31.9	62	−2.6	5.0	−20.7
24	−6.0	6.1	−30.2	63	−3.5	7.7	−20.2
25	−6.0	5.4	−39.7	64	−2.6	11.1	−19.5
26	−4.5	8.8	−27.6	65	−2.1	11.1	−22.3
27	−1.4	14.0	−29.0	66	1.6	4.4	−15.7
28	−0.6	9.9	−26.1	67	−3.5	8.1	−19.2
29	−2.5	9.2	−25.1	68	−4.2	12.0	−18.7
30	−3.5	10.4	−23.2	69	−5.5	10.7	−17.8
31	−0.5	1.8	−11.6	70	−0.2	1.8	0.8
32	−1.5	0.8	−11.5	71	−4.0	−1.7	−4.7
33	−2.5	1.7	−13.3	72	−3.8	2.2	−4.0
34	−2.6	6.3	−13.3	73	−3.8	1.0	−6.8
35	−2.8	6.8	−12.7	74	−1.4	2.2	−11.6
36	0.2	1.7	−14.3	75	1.9	2.7	−8.4
37	1.0	4.2	−29.9	76	2.8	4.6	−12.3
38	−3.1	5.1	−23.5	77	2.2	7.2	−12.8
39	−3.1	6.8	−23.9	78	−4.5	9.5	−11.7

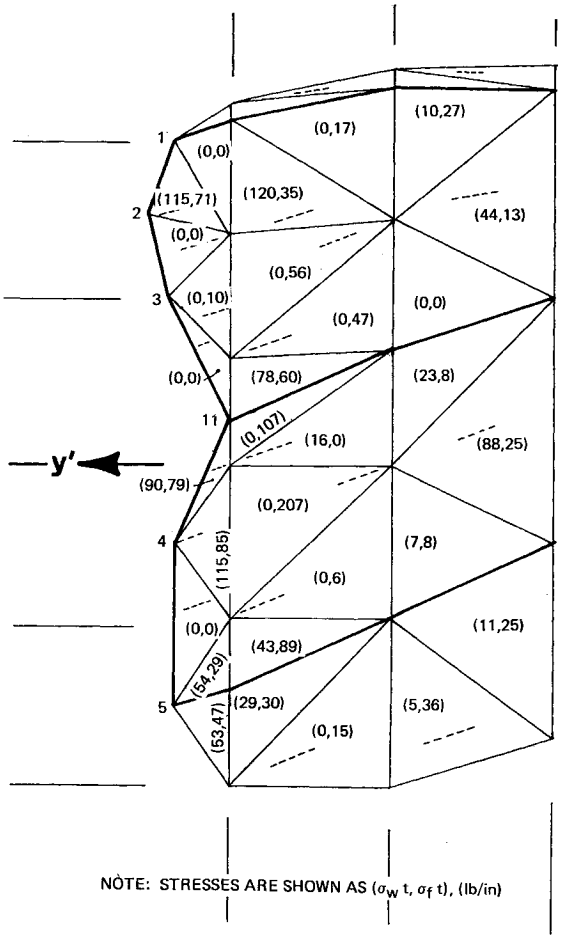

Fig. 6 Critical stress region for parawing.

compression was first reached, monotonic convergence of element stresses was obtained when the tape stresses for the first step were overestimated.

Referring to Table 4, the elements for which compressive stresses were predicted are denoted by a dashed line in the appropriate normal stress column. In Fig. 6, the predicted compressive stresses are denoted by a zero value. The dashed lines in the shear stress columns of Table 4 indicate that this stress is negligible. The abnormally large stresses predicted for elements in the neighborhood of elements 71 and 91 are a consequence of the incompatibility of the geometry and aerodynamic loading conditions. That is, these elements are resisting a rotation of the canopy as a whole about the z' axis. Such a rotation did not occur in the flight test. However, this should have little effect on the stress distribution in the region where the failure occurred, since this region is fairly remote from the overstressed elements.

Finally, it should be noted that for a system such as this, which has no geometry-defining boundary conditions, the importance of first step convergence to the validity of the subsequent steps of a linear-incremental solution cannot be over-emphasized. No satisfactory piecewise-linear solution can be accumulated for a monotonically increasing loading unless the stress and displacement increments are also monotonic. This fact was rediscovered on several occasions in the present analysis. In particular, solutions of the basic linear-incremental type, as well as types *A* and *B*, were attempted from various initial states for which complete convergence had not been obtained. None of these attempts was successful.

Conclusions

The nodal displacements, reactions, and element stresses for a finite element representation of the right lobe of a NASA parawing have been determined for the critical (failure) geometry and aerodynamic loading defined by a previous flight data analysis. Nonlinear, anisotropic material properties were used in the triangular membrane elements representing the parawing fabric. These material properties were obtained from NASA test data.

A piecewise-linear iteration technique was used to obtain the solution. This approach was made necessary by the lack of convergence in several attempts to solve the problem by the linear-incremental method. Although the iterative solution converged only approximately, the results predicted stress levels sufficient to cause failure in the region where a failure was experienced in the drop test. Furthermore, a probable cause of failure (lack of suspension lines at all reinforcement tapes) was indicated. However, failure stress levels were predicted in several elements which did not fail in the test.

The problems with convergence which were experienced in the solution are thought to be primarily the result of the asymmetric geometry and loading conditions, and the resulting tendency of certain elements to go into compression.

It was found that for an essentially free system like the parawing, first step convergence is absolutely essential for a successful incremental solution. For this reason, it is felt that additional work relative to the search for an initial tension state is required before parawing-like systems can be considered amenable to rigorous structural analysis.

References

[1] Rogallo, F. M., Lowry, J. G., Croom, D. R., and Taylor, R. T., "Preliminary Investigation of a Paraglider," TND-443, 1960, NASA.

[2] Sleeman, W. C., Jr. and Gainer, T. G., "Status of Research on Parawing Lifting Decelerators," *Journal of Aircraft*, Vol. 6, No. 10, Sept.–Oct. 1969, pp. 405–409.

[3] Gainer, T. G., "Investigation of Opening Characteristics of an All-Flexible Parawing," TND-5031, 1969, NASA.

[4] Moore, R. H., Eichblatt, D. L., and Hughes, T. F., "Experimental Scale Factors for Parawing Opening Characteristics with Dimensional Ratios from 1:1.3 to 1 : 3," TND-5071, 1969, NASA.

[5] Kenner, P. M., Churchill, F. T., and Holt, R. B., "Geometric, Aerodynamic, and Kinematic Characteristics of Two Twin Keel Parawings During Deployment," CR-1788, 1971, NASA.

[6] Alley, V. L., Jr. and Faison, R. W., "Decelerator Fabric Constants Required by the Generalized Form of Hook's Law," *Journal of Aircraft*, Vol. 9, No. 3, March 1972, to be published.

[7] Turner, M. J., Clough, R. W., Martin, H. C., and Topp, L. J., "Stiffness and Deflection Analysis of Complex Structures," *Journal of the Aeronautical Sciences*, Vol. 23, No. 9, Sept. 1956, pp. 805–823.

[8] Zienkiewicz, O. C. and Cheung, Y. K., *The Finite Element Method in Structural and Continuum Mechanics*, McGraw-Hill, London, 1967.

[9] Martin, H. C., "On the Derivation of Stiffness Matrices for the Analysis of Large Deflection and Stability Problems," *Proceedings of the Conference on Matrix Methods in Structural Mechanics*, AFFDL-TR-66-80, 1966, Air Force Fluid Dynamics Lab., Wright-Patterson Air Force Base, Ohio, pp. 697–716.

[10] Boit, M. A., *Mechanics of Incremental Deformations*, Wiley, New York, 1965.

[11] Przemieniecki, J. S., "Discrete Element Methods for Stability Analysis of Complex Structures," *The Aeronautical Journal*, Vol. 72, No. 696, Dec. 1968, pp. 1077–1086.

[12] Ambartsuman, S. A., "Theory of Anisotropic Shells," TTF-118, 1964, NASA.